The propagation of internal solitary waves over variable topography in a horizontally two-dimensional framework

CHUNXIN YUAN*, ROGER GRIMSHAW AND EDWARD JOHNSON

Department of Mathematics, University College London, London, WC1E 6BT, UK

XUEEN CHEN

College of Oceanic and Atmospheric Sciences, Ocean University of China, Qingdao 266100, China

**Corresponding author address:* Chunxin Yuan, Department of Mathematics, University College London, London, WC1E 6BT, UK

E-mail: chunxin.yuan.14@ucl.ac.uk

ABSTRACT

In this paper we present a horizontally two-dimensional theory based on a variable-coefficient Kadomtsev-Petviashvili equation, which is developed to investigate oceanic internal solitary waves propagating over variable bathymetry, for general background density stratification and current shear. To illustrate the theory, we use a typical monthly averaged density stratification, for the propagation of an internal solitary wave over either a submarine canyon or a submarine plateau. The evolution is essentially determined by two components, nonlinear effects in the main propagation direction, and the diffraction modulation effects in the transverse direction. When the initial solitary wave is located in a narrow area, the consequent spreading effects are dominant, resulting in a wave field largely manifested by a significant diminution of the leading waves, together with some trailing shelves of the opposite polarity. On the other hand, if the initial solitary wave is uniform in the transverse direction, then the evolution is more complicated, albeit can be explained by an asymptotic theory for a slowly varying solitary wave combined with the generation of trailing shelfs needed to satisfy conservation of mass. This theory is used to demonstrate that it is the transverse dependence of the nonlinear coefficient in the Kadomtsev-Petviashvili equation rather than the coefficient of the linear transverse diffraction term which determines how the wave field evolves. The MIT general circulation model is used to provide a comparison with the variable-coefficient Kadomtsev-Petviashvili model, and we find good qualitative and quantitative agreements.

1. Introduction

Interest in the nonlinear internal solitary waves (ISWs) that occur in the coastal ocean has been particularly strong during the last several decades owing to their important role on the marine ecosystem, marine geology and in coastal engineering. ISWs often have large amplitudes and strong currents, for instance, Huang et al. (2016) recorded an extreme ISW with an amplitude of $240\,m$ and a peak westward current velocity of $2.55\,ms^{-1}$ in the northern South China Sea. The scale of these waves implies that they could pose potential hazards for underwater drilling, see Osborne et al. (1978). Moreover, the ability of these internal waves to propagate horizontally provides a mechanism for the transport of energy and momentum over large distances.

A large number of observations demonstrate the existence of ISWs in numerous locations around the world's ocean, both from the perspective of field measurements in Farmer and Smith (1978); Sandstrom and Elliott (1984); Ramp et al. (2004); Shroyer et al. (2010); Huang et al. (2016) and remote sensing images in New and Da Silva (2002); Zhao et al. (2004); Da Silva et al. (2009); Liu et al. (2013). These observations, together with numerical simulations (see Vlasenko and Stashchuk (2007) for instance), illustrate that due to the complicated and essentially two-dimensional (2D) bathymetry, wave refraction and diffraction can occur, indicating that the horizontal 2D effect is important and in some circumstances cannot be ignored, especially when there are strong variations in the transverse direction.

The Korteweg-de Vries (KdV) equation embodying the cumulative and competing nonlinear and dispersive effects is commonly used to investigate internal waves in the coastal ocean, see Helfrich and Melville (2006); Ostrovsky and Stepanyants (2005) or the book by Vlasenko et al. (2005). There are various extensions, such as the variable-coefficient KdV equation and the extended KdV equation with a cubic nonlinear term, see Lamb and Yan (1996); Grimshaw et al. (1997, 2004, 2007, 2010) and the references therein. In the present context, an important extension from one to two horizontal space dimensions is the Kadomtsev-Petviashvili (KP) equation, which describes weakly nonlinear, long waves propagating along a predominant direction (say the positive x direction) in a 2D domain, see Kadomtsev and Petviashvili (1970) for the original derivation, and the subsequent work by Johnson (1980); Katsis and Akylas (1987); Grimshaw and Melville (1989). However, these works and other more recent studies took a constant depth assumption, which, to some degree, limits its practical application, so several extended KP equations have been derived to take additional physical background factors into account, albeit we note that the general derivation by Grimshaw (1981) allowed for variable depth, and also for horizontally varying background density and current fields. Although a large amount of closely related work has been done in many physical settings, for instance on surface waves in shallow water, see the review by Akylas (1994), our attention here will be confined to internal waves. A further extension to take account also of the Earth's background rotation leads to the rotation-modified KP equation, Grimshaw (1985) for the case of internal waves in a rotating constant-depth channel. Taking the effect of rotation and a steady background current into account, Chen and Liu (1995) derived a unified KP equation for surface and interfacial waves propagating in a channel with varying topography and sidewalls.

In summary, for internal waves, the existing KP-type equations are able to take one or some of the effects of rotation, background current, varying topography and also boundary walls into consideration, but nonetheless many of them are still based on model density stratifications, such as a two-layered system. Especially we note that Pierini (1989) used the two-layered so-called regularised long wave equation, a slightly different version of the KP equation, to simulate internal solitary waves in the Alboran Sea under some quite simple assumptions, namely that there is no background rotation, that the topography is constant, that the interface depth is constant and that there is no background current. Subsequently Cai and Xie (2010) invoked a similar model, again in the configuration of two-layered fluid, to investigate the propagation of ISWs in the northern South China Sea. Despite the apparent simplicity of the two-layered model and its wide adoption, the oceanic density stratification is better represented as continuous when examining oceanic scenarios, see Grimshaw et al. (2017) for instance. The main objective of this paper is to describe and use a new variable-coefficient KP equation, which is based on quite general continuous density stratification, and importantly has variable 2D topography. The basis of this model was first proposed by Grimshaw (1981) in a theoretical analysis, and here we develop it further for use in practical applications, and also provide some supplementary analyses. A detailed comparison between *in situ* observations and our presented theory is not shown here, as it is difficult to follow the space-time evolution of observed ISWs in detail. Instead we compare numerical simulations of the KP model with those from the fully nonlinear and non-hydrostatic MIT general circulation model (MITgcm). We focus on two scenarios, propagation of ISWs over a canyon and propagation over a submarine plateau.

In Section 2, we present the variable-coefficient KP equation, together with some preliminary analysis of how variable 2D topography affects the propagation of ISWs. In Section 3, we describe a numerical scheme incorporating both a finite difference and a pseudo-spectral method to solve this equation accurately, and this is followed by the numerical simulations for the propagation of ISWs over a submarine canyon and over a submarine plateau. In Section 4 we describe the set-up and analogous results from the MITgcm model. We conclude with a discussion in Section 5.

2. Formulation

a. Kadomtsev-Petviashvili equation

In the absence of dissipation and background rotation, and in a uniform background environment, that is the topographic depth is constant and the background density field and current do not vary horizontally, the KP equation in the usual physical variables pertinent to oceanographic applications is given by, see Grimshaw (1981, 1985) and the review by Helfrich and Melville (2006),

$$\{A_t + cA_x + \alpha AA_x + \beta A_{xxx}\}_x + \frac{\gamma}{2}A_{yy} = 0\,, \tag{1}$$

where $A(x,y,t)$ is the amplitude of the wave, x, y and t are space and time variables respectively, and subscripts denote derivatives. Here x is chosen to be along the primary wave propagation direction, where the waves have a linear long-wave phase speed c, while y is the transverse direction where there are weak diffraction effects. The nonlinear coefficient α, and dispersive coefficients β, γ are determined by the waveguide properties, and for the specific oceanic application, are defined below.

To leading order in an asymptotic expansion, the vertical particle displacement relative to the basic state is

$$\zeta(x,y,z,t) = A(x,y,t)\phi(z), \tag{2}$$

where $\phi(z)$ is the modal function, defined by

$$\left\{\rho_0\,(c-u_0)^2\,\phi_z\right\}_z + \rho_0 N^2\phi = 0\,, \quad \text{for} \quad -h < z < 0\,, \tag{3}$$

$$\phi = 0 \quad \text{at} \quad z = -h\,, \quad (c-u_0)^2\,\phi_z = g\phi \quad \text{at} \quad z = 0\,. \tag{4}$$

Here $\rho_0(z)$ is the background density distribution of a stable stratified fluid, which is mostly characterised by the buoyancy frequency N, represented by $\rho_0 N^2 = -g\rho_{0z}$, and $u_0(z)$ is a background horizontal shear flow. Note that if the rigid lid approximation is assumed, then the free surface boundary condition is replaced by $\phi = 0$ at $z = 0$. Then the coefficients α and β in equation (1) are given by the usual expressions as for the well-known KdV equation,

$$I\alpha = 3\int_{-h}^{0} \rho_0\,(c-u_0)^2\,\phi_z^3\,dz\,, \tag{5}$$

$$I\beta = \int_{-h}^{0} \rho_0\,(c-u_0)^2\,\phi^2\,dz\,, \tag{6}$$

$$I = 2\int_{-h}^{0} \rho_0\,(c-u_0)\,\phi_z^2\,dz\,, \tag{7}$$

whereas the coefficient γ is given by $\gamma = c$ when there is no shear flow, $u_0(z) \equiv 0$, but when there is a shear flow it is given by

$$I\gamma = I_2\,, \quad I_2 = 2\int_{-h}^{0} \rho_0(c-u_0)^2\phi_z^2\,dz\,. \tag{8}$$

The KP equation (1) has two important conservation laws,

$$\int_{-\infty}^{+\infty} A\,dx = [B]_{-\infty}^{+\infty} = f(t)\,, \quad B_x = A\,, \tag{9}$$

$$\frac{\partial}{\partial t}\int_{-\infty}^{+\infty} \frac{A^2}{2}\,dx + \frac{\gamma}{2}\frac{\partial}{\partial y}\int_{-\infty}^{+\infty} AB_y\,dx = 0\,, \tag{10}$$

for solutions $A(x,y,t)$ localized (or periodic) in x. They represent the conservation of mass and wave action flux respectively.

b. Variable background

When the depth h, background current u_0 and density ρ_0 vary slowly with x and y, the KP equation (1), see Grimshaw (1981), is replaced by the variable-coefficient KP (vKP) equation

$$\{A_t + cA_x + \frac{cQ_x}{2Q}A + \alpha AA_x + \beta A_{xxx}\}_x + \frac{\gamma}{2}A_{yy} = 0\,, \tag{11}$$

where $Q = c^2 I$ is the linear magnification factor, usually scaled to

$$\bar{Q} = \frac{c^2 I}{c_0^2 I_0}\,, \tag{12}$$

where the subscript 0 indicates the values at a specific location, say $x = x_0$ where Q is normalised to be unity, and hereafter we will omit the $\bar{\ }$. The modal function ϕ and speed c now depend and hence the coefficients α, β, γ also depend (slowly) on both x and y. The derivation of the evolution equation (11) requires the introduction of two small parameters δ and ε, respectively characterising the wave amplitude and dispersion, and they relate to each other by $\delta = \varepsilon^2$ in the usual KdV balance. Then to leading order of the asymptotic analysis, see Grimshaw (1981), the amplitude is $\varepsilon^2 \widehat{A}(\varepsilon x, \varepsilon^2 y, \varepsilon t)$ and the coefficients depend on the slow variables $\hat{x} = \varepsilon^3 x$ and $\hat{y} = \varepsilon^3 y$. As a consequence, to keep the vKP equation (11) in a valid asymptotic regime, in essence, the y-variations should be suppressed *vis-a-vis* the x-variations, since x is the dominant direction. Although this property might seem to impose another limitation on any application, in practice this is often the situation in the real ocean, that is, if the wave propagation direction is selected to be x, then the variations along the transverse y direction are much smaller. Also note that the derivation of the vKP equation by Grimshaw (1981) was along the ray path determined by the linear long wave speed c, and then taking account of diffraction relative to this ray. But here we choose the x-direction as the ray, consistent with our choice of topography being symmetric about that axis.

It is now useful for both analysis and numerical simulation, to transform equation (11) to a more convenient "spatial" evolution form,

$$X = \int_{x_0}^{x} \frac{dx}{c} - t\,, \quad T = \int_{x_0}^{x} \frac{dx}{c}\,. \tag{13}$$

Then to leading order of the asymptotic approximation,

$$\{A_T + \frac{Q_T}{2Q} A + \mu A A_X + \lambda A_{XXX}\}_X + \frac{\sigma}{2} A_{yy} = 0\,, \tag{14}$$

$$\mu = \frac{\alpha}{c}\,, \quad \lambda = \frac{\beta}{c^3}\,, \quad \sigma = c\gamma\,. \tag{15}$$

All terms are now of the same order, that is, $A \sim \varepsilon^2$, $\partial/\partial X \sim \varepsilon$, $\partial/\partial T \sim \varepsilon^3$, $\partial/\partial y \sim \varepsilon^2$. Here the coefficients μ, λ, σ, Q depend on T and y, but note that the y-dependence in these coefficients is order $\mathscr{O}(\varepsilon^3)$, much slower than the y-variation of A, which is order $\mathscr{O}(\varepsilon^2)$ formally. Further simplifications are

$$U = A\sqrt{Q}\,, \quad \{U_T + \frac{\mu}{Q^{1/2}} U U_X + \lambda U_{XXX}\}_X + \frac{\sigma}{2} U_{yy} = 0\,. \tag{16}$$

Without loss of generality, we can assume that the wave propagate in the positive x-direction, so that $\lambda > 0$. Then (16) can be further transformed exactly to

$$\{U_\varsigma + \nu U U_X + U_{XXX}\}_X + \tau U_{yy} = 0\,, \tag{17}$$

$$\text{where} \quad \varsigma = \int_0^T \lambda(T')\,dT'\,, \quad \nu = \frac{\mu}{\lambda\sqrt{Q}}\,, \quad \tau = \frac{\sigma}{2\lambda}\,. \tag{18}$$

The vKP equation (17) can be written in a form of a "forced" KdV equation,

$$U_\varsigma + \nu U U_X + U_{XXX} + \tau V_{yy} = 0\,, \quad V_X = U\,, \quad V = -\int_X^{+\infty} U(X', y, \varsigma)\,dX'\,. \tag{19}$$

Here it is assumed that $V \to 0$ as $X \to +\infty$ since small amplitude waves all propagate in the negative X-direction. The vKP equation (19) has two conservation laws, analogous to (9, 10),

$$\int_{-\infty}^{+\infty} U\,dX = [V]_{-\infty}^{+\infty} = 0\,, \tag{20}$$

$$\frac{\partial}{\partial\varsigma}\int_{-\infty}^{+\infty} \frac{U^2}{2}\,dX + \tau\frac{\partial}{\partial y}\int_{-\infty}^{+\infty} U V_y\,dX = 0\,, \tag{21}$$

for solutions $U(X, y, \varsigma)$ localised (or periodic) in X. Note that four expressions of the vKP equation are available, that is (11, 16, 17, 19), of which (16, 17, 19) are exactly equivalent, while (11) is asymptotically equivalent to each. Which one should be chosen depends on the specific application. For example, if the intention is to make comparisons with the data captured from a fixed mooring site, then the form (16) could be used, and no extra interpolations are needed. But for numerical simulations of a process model as here, and analytical analyses, the form (17) is recommended as all the variability is represented by just two coefficients ν and τ.

It is useful to clarify here the relationship between the wave amplitude in the transformed space and the wave amplitude in the physical space. For a solitary wave in the transformed space (X, y, ς), along a fixed y section line ($y = 0$ for instance), the maximum amplitude at "time" ς can be expressed as

$$U_m = U(\varsigma, X_m(\varsigma)), \quad \text{where} \quad U_X = 0 \text{ at } X = X_m(\varsigma), \tag{22}$$

where $|U_m|$ is a local maximum, and the y-dependence is suppressed. Analogously in the physical space, the maximum amplitude at the location x is written as

$$A_m = A(t_m(x), x), \quad \text{where} \quad A_t = 0 \text{ at } t = t_m(x), \tag{23}$$

where $|A_m|$ is a local maximum. Then since $U = A\sqrt{Q}$ (16), and using the transforms (13),

$$\lambda U_\varsigma = (A\sqrt{Q})_t + c(A\sqrt{Q})_x, \quad U_X = -(A\sqrt{Q})_t\,. \tag{24}$$

Since here it transpires that the variation of Q is quite small, see figure 6 in our cases, we see that the maximum in the transformed and physical spaces approximately coincide. Importantly, note that the maximum in the transformed space is a maximum over X at a fixed "time" ς, and this coincides, modulo any small variation in Q, with a maximum over time t in the physical space at a fixed location x, such as would be observed at a fixed mooring site.

c. Slowly varying solitary waves

One of the basic assumptions of this vKP model is that the y-variations should be sufficiently slow relative to a typical solitary wave scale in the x-direction. This suggests an asymptotic analysis for a slowly varying solitary wave solution of (17) represented by,

$$U \sim a\,\mathrm{sech}^2\{\kappa[X - P(y,\varsigma)]\}, \quad W = P_\varsigma = \frac{\nu a}{3} = 4\kappa^2, \tag{25}$$

$$V = -\int_X^{+\infty} U\,dX = \frac{a}{\kappa}\{\tanh[\kappa(X - P)] - 1\}\,. \tag{26}$$

In this scenario, the amplitude a and hence the wavenumber κ and the nonlinear phase speed W vary slowly with y, ς. Note that (25) is defined in a reference frame with linear phase speed c, so that from the mappings (13, 18), the total phase speed in the physical space is $c_{sol} = c(1-W\lambda)^{-1} \approx c(1+W\lambda)$ since the solitary wave amplitude is required to be small. Using the transformations in (13, 18) $c_{sol} = c + \alpha a_{sol}/3$ where $a_{sol} = a/Q^{1/2}$ as expected. To determine the variation on the amplitude it is sufficient to substitute (25) into the conservation law (21), with the outcome

$$\left(\frac{2a^2}{3\kappa}\right)_\varsigma = \tau\left[\frac{4a^2}{3\kappa}P_y + (\frac{a^2}{\kappa^2})_y\right]_y . \tag{27}$$

Using the relations that $\nu a = 12\kappa^2, P_\varsigma = 4\kappa^2$ this reduces to

$$\left(\frac{\kappa^3}{\nu^2}\right)_\varsigma = \tau\left[\frac{2\kappa^3}{\nu^2}P_y + (\frac{3\kappa^2}{2\nu^2})_y\right]_y , \quad P_\varsigma = 4\kappa^2 , \tag{28}$$

which can be written in the convenient form,

$$\theta_\varsigma = \tau\left[2\theta P_y + (\frac{3\theta^{2/3}}{2\nu^{2/3}})_y\right]_y , \quad P_\varsigma = 4\nu^{4/3}\theta^{2/3} , \quad \theta = \frac{\kappa^3}{\nu^2} . \tag{29}$$

This is a nonlinear mixed hyperbolic-parabolic type system for θ, P, where the first term on the right-hand side of the first equation generates the hyperbolic part and the second term generates the parabolic part. It seems quite difficult to obtain an analytical solution, and hence in the following sections we will numerically solve this equation system with the constant initial condition that $\theta = \theta_0, P = P_0$.

When there are no y-variations, equation (29) reduces to the well-known adiabatic law θ is a constant, that is $\kappa \propto |\nu|^{2/3}$ and so $a \propto |\nu|^{1/3}$. However when there are y-variations, then we note that the y-dependence in the coefficients ν, τ can be taken as parametric, consistent with the assumptions made in the derivation of the vKP equation (11). Assuming here without loss of generality that $\nu > 0$, the system (29) can be simplified to an asymptotically equivalent form

$$\theta_\varsigma = \frac{\tau}{\nu^{2/3}}\left[2\theta\nu^{2/3}P_y + (\frac{3\theta^{2/3}}{2})_y\right]_y, \quad \theta = \frac{\kappa^3}{\nu^2}, \quad P_\varsigma = 4\nu^{4/3}\theta^{2/3}. \tag{30}$$

But further analytical progress still seems quite difficult without further approximation. Hence, to provide some insight into the structure of the solutions, we linearise this system with respect to the "constant" state $\theta = \theta_0$, noting that this is the adiabatic solution $\kappa \propto \nu^{2/3}$, and so put $\theta = \theta_0 + \tilde{\theta}$. Linearisation then yields

$$\tilde{\theta}_\varsigma = 2\tau\theta_0\tilde{P}_{yy} + \frac{\tau}{\nu^{2/3}\theta_0^{1/3}}\tilde{\theta}_{yy}, \quad \tilde{P}_\varsigma = \frac{8\nu^{2/3}}{3\theta_0^{1/3}}\tilde{\theta}. \tag{31}$$

The first term on the right-hand side generates a linear hyperbolic equation and small disturbances propagate outward in the y-direction with a speed $y/\varsigma \sim \nu^{1/3}\theta_0^{1/3}(16\tau/3)^{1/2}$, whereas the second term on the right-hand side generates a linear diffusion equation with a diffusion scale y_d where $y_d^2/\varsigma \sim \tau/(\nu^{2/3}\theta_0^{1/3})$, and it is apparent these two terms together constitute the spreading effect in the y-direction. This analysis is similar to that of Kadomtsev and Petviashvili (1970) for the stability of a KdV solitary wave to transverse modulations, but more generally, here it demonstrates the extension of that result to the vKP equation (17).

As in the well-known KdV theory for a slowly-varying solitary wave, this asymptotic solution does not conserve the mass invariant (20), and the resolution is that as the solitary wave deforms a trailing shelf is generated to conserve the total mass. This trailing shelf is essentially a linear long wave of small amplitude but long wavelength and so can carry mass of the same order as that of the solitary wave. The solitary wave mass is $2a/\kappa$ and this varies as $24\theta^{1/3}\nu^{-1/3}$. Relative to the constant state $\theta = \theta_0$, it follows that when ν increases (decreases), the solitary wave amplitude $a = 12\nu^{1/3}\theta^{2/3}$ increases (decreases), then the trailing shelf has the same (opposite) polarity as the solitary wave. However, note that this conclusion could change if θ also has significant variations in the y-direction.

3. Two-dimensional topographic effects

a. Model set-up

As noted in the Introduction, 2D effects will be especially significant in an area with an abrupt change in the oceanic background state, such as in the bathymetry, or in the background density and current fields. A typical instance is the New York Bight, which is characterised by a large area of continental shelf containing the Hudson Canyon, see figure 1. This area is also affected by the strong Gulf Stream current, as well as by coastal river inflow, and all these factors together make the local wave dynamics quite complicated. As ISWs propagate up the shelf from deep water, and pass through the Hudson Canyon, we expect that wave diffraction and refraction will occur. Motivated by this and similar examples we set up an idealised undersea canyon-type topography $h(x,y)$ with typical oceanic length scales, see figure 2,

$$h = \frac{\tanh\Omega + 1}{2} \cdot (h_1 - h_2) + h_2\,, \tag{32}$$

$$\text{where} \quad \Omega = \frac{K_2 - K_1 M_y}{x_1 - x_0} \cdot (x - x_0) + K_1 M_y\,, \tag{33}$$

$$\text{and} \quad M_y = \left[\tanh\left(\frac{y + y_{ts}}{y_{tw}}\right) - \tanh\left(\frac{y - y_{ts}}{y_{tw}}\right)\right] \cdot L_y + 1.0\,. \tag{34}$$

Here we set $y_{ts} = 6000\,m$, $y_{tw} = 2000\,m$, $L_y = 0.7$, $K_1 = -2.7$, $K_2 = 2.7$, and the topography is confined in a domain with size $x \times y = [0:80] \times [-40:40]\,km^2$, so that two edges in the x direction are $x_0 = 0$ and $x_1 = 80\,km$, while the water depth parameter $h_1 = 350\,m$ and $h_2 = 500\,m$ respectively. We also consider an idealized plateau-type topography, see figure 2, whose expression is the same as that of the canyon case, except that

$$M_y = \left[\tanh\left(\frac{y - y_{ts}}{y_{tw}}\right) - \tanh\left(\frac{y + y_{ts}}{y_{tw}}\right) + 2\right] \cdot L_y + 1.0\,. \tag{35}$$

Using these idealized topographies makes it feasible to conduct analytical work in the sequel. Although realistic topography is not considered here, we contend the framework used here can be easily and effectively migrated to the implementation of real topography, whose transverse variation is relatively slower than that in the wave propagation direction. Further, as customary, since the surface disturbances induced by ISW are usually very small (typically $\mathscr{O}(10^2)$ smaller), we make the rigid lid approximation, and also set the background current, $u_0(z) \equiv 0$. The background temperature and salinity profiles are the monthly averaged data from the World Ocean Atlas 2013. We choose data in July at 37.5°N, 72.5°W, in the vicinity of the Hudson Canyon, which is shown in figure 3.

When examining 2D effects, another important issue is the preparation of the initial condition. To simulate the waves from a generation site, here we select the well-known KdV solitary wave but with a y-envelope imposed,

$$U(X,y,\varsigma=0) = E(y)\left\{a_0\,\mathrm{sech}^2\left[\kappa_0(X-X_0)+D(X)\right]\right\}, \quad \nu_0 a_0 = 12\kappa_0^2\,. \tag{36}$$

Here X_0 is chosen to place the solitary wave in the deep water where $\nu = \nu_0$. $E(y)$ is an envelope function in the transverse y direction, equal to unity in a specified region $|y| < L$ and tapering to zero outside that range,

$$E(y) = \frac{1}{2}\{\tanh(\frac{y+y_e}{y_w}) - \tanh(\frac{y-y_e}{y_w})\}\,. \tag{37}$$

Note that the attenuation in the y-direction should be greater than that in the X-direction, so we choose $y_w \gg 1/\kappa_0$, and also we require $y_e \gg y_w$ to ensure a large value of L. To isolate the dynamics of the 2D topography, we also did simulations with a y-independent initial condition, that is $E(y) \equiv 1$. The mass constraint (20) must be satisfied, which implies that in the Fourier space, solutions have no energy at the zero wavenumber. As a consequence, a pedestal $D(X)$ needs to be superimposed on the KdV solitary wave. For a numerical domain of total length $2L_X$ in the X direction, the simplest choice is $D(X) = -12\kappa_0/(\nu_0 L_X)$, so that the initial mass is zero,

$$\int_{-\infty}^{\infty}\left\{a_0\,\mathrm{sech}^2[\kappa_0(X-X_0)] + D(X)\right\}dX = \frac{2a_0}{\kappa_0} - \frac{24\kappa_0}{\nu_0} = 0\,. \tag{38}$$

The expression (38) is a good choice for a periodic domain. However because here two sponge layers are deployed at the two edges of the X-domain (details below), a form with an envelope which avoids possible end effects is used,

$$D(X) = \frac{D_0}{2}\{\tanh(\frac{X+L_e}{L_w}) - \tanh(\frac{X-L_e}{L_w})\}, \quad \int_{-\infty}^{\infty} D(X)\,dX = 2D_0 L_e = -\frac{24\kappa_0}{\nu_0}. \tag{39}$$

In principle, the lengths L_e and L_w can be chosen freely, but to facilitate the numerical calculations, it is better to keep the pedestal small, that is to say $|D_0| \ll a_0$, and hence $|\kappa_0| L_e \gg 1$, so one combination of the typical values is $L_e = L_X/2, L_w = L_X/4$.

The asymptotic theory developed in section c can be applied to estimate the deformation of the solitary wave amplitude a, ignoring any effect of the small pedestal. First, we use the asymptotic solution for $\theta \sim \theta_0$ in equation (30) where $\theta^2 \propto a^3/\nu$ to estimate that overall the amplitude a will deform adiabatically as $|\nu|^{1/3}$, with a consequent effect on the phase speed. In the physical variables x,t this is $c/(1-W\lambda) \approx c(1+W\lambda)$ since $W = \nu a/3 \sim |\nu|^{4/3}$ is a small perturbation. Then, in addition, the effect of the envelope function $E(y)$ can be estimated using the linearised system (31). It is clear that the main variation will then come from the end-points $y = \pm y_e$ of the envelope. These will generate small disturbances propagating in the y-direction with speeds proportional to $\nu^{1/3}\theta_0^{1/3}(16\tau/3)^{1/2}$, and at the same time diffusing on a length scale y_d where $y_d^2/\varsigma \sim \tau/(\nu^{2/3}\theta_0^{1/3})$. Both processes are enhanced as the initial wave amplitude increases through the dependence on $\theta_0^{2/3} \propto a_0$, and also enhanced as y_w decreases, that is sharper fronts at the ends of $E(y)$.

b. Numerical method and results

Although the formulation of the vKP equation (11) is for any mode, in this paper we focus on only mode-1 waves, which are the most commonly observed in the ocean, although there are some observations of mode-2 waves, see for instance, Shroyer et al. (2010); Liu et al. (2013). Using the background profiles shown in figures 2 and 3, the nonlinear coefficient $\nu < 0$, see figure 5, indicating that mode-1 ISWs are waves of depression. To ensure the simulations are in the weakly nonlinear regime, here we choose $-15\,m$ as the initial amplitude in all cases.

The numerical simulations are carried out in the transformed space, using the vKP equation (17). A pseudo-spectral method based on a Fourier interpolant is used in the primary wave propagation (that is X here) direction, and the dispersion along the y direction is simulated by a fourth order central finite difference scheme, while a classical Runge-Kutta fourth-order method, together with a very fine time step, provides an accurate outcome in the time domain. Two sponge layers are added in the X direction to absorb the incident waves and so avoid any reflection, while in the y direction, when $E(y) \equiv 1$ then a periodic boundary condition is used, otherwise two sponge layers are deployed at edges as that in the X direction. Once the results have been obtained in the transformed space, a 2D interpolation is implemented to transform back to the physical space, that is, from U in equation (17) to A in (11) or (14). Clearly the interpolation will introduce some further errors, but they are found with some experimentation to be quite small and can be ignored, and the following quantitative comparisons with the MITgcm model will put this claim on a firmer footing, see figure 11. Note that the essential dynamics takes place in the transformed space, and the mapping back to the physical space can only change the amplitude magnitudes in the evolving wave field, and cannot by itself generate new wave features, since $U = A\sqrt{Q}$ (16) and the transformations (13) affect only the time and space scales. Note especially that the profile for U in the X-space at a fixed "time" ς corresponds to a time series for A at a fixed place x, see (24).

In both cases of the undersea canyon-type and plateau-type topography, the initial solitary wave with the envelope $E(y)$ defined in (37) immediately disperses along the transverse y direction when the simulations start, and importantly the wave fronts are not straight, but instead are curved backwards relative to the x direction, see figure 4. This is because the local phase speed is a function of the local wave amplitude, which decays on both sides away in the y-direction from the initial main wave centred at $y = 0$. This permanent cross-domain dispersion results in a dramatic decrease of the amplitude of the main wave with distance in the x-direction of propagation. On the other hand, after propagating away from the flat bottom and up the slope, the waves also begin to deform in the x-direction due to the effect of the nonlinear coefficient ν in (17) which combines the physical nonlinear coefficient α with the physical linear dispersive coefficient β, and also absorbs the magnification factor Q, see figure 6. The asymptotic theory developed in section c predicts the deformation of the main wave is determined by two components in the mapping space, that is, the terms related with ν and τ respectively, see equation (30). More specifically, let us focus on the central line in the y direction, that is $y = 0$. Figure 5 shows that along the propagation direction $|\nu|$ increases, and hence the amplitude of the evolving main wave will increase, since it deforms as $|\nu|^{1/3}/Q^{1/2}$ in the physical space, but at the same time the afore-mentioned spreading in the y-direction will lead to some amplitude decay. It turns out the latter is overwhelmingly significant and causes the wave amplitude to decay, see figure 4. To conserve the total mass, this decay generates a trailing shelf with positive polarity, and there is evidence that this shelf begins to fission into several small ISWs, see figure 11.

The features described above occur for both the canyon and plateau cases, and the main difference between these two cases is that the central part of the wave field around $y = 0$ is propagating faster over the canyon than over the plateau, see figure 4. This can be partly attributed to the topographic variations in the linear phase speed c, see figure 6, which shows that c is greater over the canyon than over the plateau. However the difference is quite small, of $\mathscr{O}(5\%)$, and comparable with the change in c from deep to shallow water, due to scaling dependence on $\sqrt{h}$. Furthermore, this effect is purely kinematic and linear, whereas the simulations of the nonlinear vKP equation

(17) are in a reference frame moving with the speed c, and will contain dynamic effects due to the amplitude-dependent phase speed W for the evolving ISW. This can be estimated from our simulations as follows. Suppose that the y-variations (the canyon or plateau) are removed from the topography, then the evolving ISW will deform according to the adiabatic law $\kappa \propto |\nu|^{1/3}$ and then $W = 4\kappa^2$, see (25). This forms a base level to determine the effect of a canyon, or plateau, on the nonlinear phase speed W. Then with the canyon or plateau topography restored we use the asymptotic expression that $\theta = \theta_0$, see (30) and the accompanying discussions. Of course, this adiabatic estimate is within the confines of a slowly-varying assumption, so that at fixed "time" ς, the state θ is asymptotically equivalent no matter whether or not there are y-variations in the background topography. Then from equation (30) we get that

$$\frac{W_c}{W_r} = \left(\frac{\nu_c}{\nu_r}\right)^{4/3} \quad \text{and} \quad \frac{W_p}{W_r} = \left(\frac{\nu_p}{\nu_r}\right)^{4/3}, \tag{40}$$

where the subscript r indicates the reference level without y-variations, while c and p indicate the canyon and plateau case respectively. The results of (40) are shown in figure 7. Initially, the waves are over the flat bottom where there are no y-variations, but with the propagation up the slope, which will then become more and more significant. We note immediately an important consequence, in view of the nonlinear effects of y-variations on W, the canyon-type topography actually slows down the propagation ($W_c/W_r < 1$), contrasting with the speed-up of the plateau-type topography ($W_c/W_r > 1$). Nevertheless, the magnitude of $W\lambda = \nu a\lambda/3$ ($\mathscr{O}(10^{-1})$) is much smaller than the corresponding linear phase speed c ($\mathscr{O}(1)$), which is to say, although the effects of the y-variations can slightly modulate the phase speed $c_{sol} \approx c(1+W\lambda)$, the linear phase speed c is still dominant, and this is precisely what is seen in figure 4 and 8.

Although the simulations shown in figure 4 are intended to describe the propagation of ISW over 2D topography in the ocean, the underlying dynamics induced by the topography alone is not very well exhibited, since it is mostly hidden by the significant y spreading induced by the truncated initial condition. In practice oceanic ISWs are limited in the transverse direction, however this scale could be quite long, and hence in figure 8 we show the simulations when the initial condition on the flat bottom before the waves reach the slope has no y-dependence, that is $E(y) \equiv 1$. The evolution of the wave again obeys the adiabatic law in the physical space, the amplitude of the leading wave $|a| \sim |\nu|^{1/3}/Q^{1/2}$, and due to mass conservation, a trailing shelf (indicated by light green colour) of the same polarity is generated. Initially, the wave evolution at the central part around $y = 0$ behave qualitatively similar to the previous cases, that is, it is largely determined by the liner phase speed c, but at the same time, is slightly modulated by the small nonlinear phase speed W, which has an opposite effect to that of c. Then after moving up the slope, the effects of the y-variations in the bathymetry become important and so the adiabatic law fails, and the y-dependence has to be taken into account in equation (28) or (29). With the gradual propagation up the slope, the waves in the canyon (plateau) propagate ahead (behind) the waves outside, and the non-adiabatic effects due to the y-variations of the topography become further enhanced, leading to a significant distinction between the wave amplitudes at different y-locations. Nevertheless, the total mass along the x direction on each y-section has to be conserved, which, together with the spreading effect in the y direction, leads to a complicated transverse modulation (shown by the dark blue colour).

To examine this explanation in more detail, a set of calculations based on the equation system (29) is shown in figure 9 where we plot the amplitude of the leading wave using the expressions for $\theta = \kappa^3/\nu^2$ in (29) and the solitary wave expression $\nu a = 12\kappa^2$ (25) so that $a = 12(\theta^2\nu)^{1/3}$. Note that the asymptotic theory (29) is based on the (21) and so conservation of wave action flux is automatically satisfied. It is apparent that in the canyon case, over the slope, the amplitude of the leading wave $|a| = 12(\theta^2|\nu|)^{1/3}$ in the canyon increases, contrasting with the decline in the periphery of the canyon. Moreover, this feature expands with "time" ς and exerts more influence on the wave field, as the asymptotic theory based on (29) predicts. Simultaneously, at the central part, the increase of the mass represented by the leading wave $24(|\theta/\nu|)^{1/3}$ leads to an opposite polarity trailing shelf (see the dark blue colour in figure 8) in order to conserve the total mass in the X direction. In contrast, the mass undergoes a decrease outside the submarine canyon, and so using the mass conservation law again, a trailing shelf of the same polarity forms, which further develops into several small ISWs (see the light green colour in figure 8). A similar interpretation can be applied to the plateau case, but with an opposite structure. As we have noted, small y-variations of the topography can lead a significant distinction through the coefficients ν and τ. In order to examine which coefficient is the more effective, we show in figure 10 calculations from the system (29) when the y-dependence of ν and then τ are separately removed. We see that when only the y-dependence of the coefficient ν is removed, the wave field is quite different from that using the full expression for ν, see figure 9. However if instead only the y-variations in τ are removed, then the wave structure is almost the same as when the full expression for τ is used. We infer that it is the y-variations in the nonlinear coefficient ν which essentially determine the evolving wave field, at least for the system parameters used here.

4. MITgcm model simulations

Access to 2D observational data which incorporates a complete shoaling process is impractical. Thus here we use instead a fully nonlinear and non-hydrostatic three-dimensional (3D) primitive equation model, MITgcm, to do both qualitative and quantitative comparisons. For details of the MITgcm model, see Marshall et al. (1997).

Since our presented KP theory is non-dissipative, the dissipation (eddy viscosity) in the MITgcm model is also set to be zero, so that formally it solves the incompressible Boussinesq equations.

The simulation domain, topography and background profiles are exactly the same as in the KP theory, see figure 2 and 3. In the x direction, 60 of a total 800 grid points at the end of the domain are designed to be a boundary layer with a decrease of resolution, telescoped exponentially from 100 to $10^4\,m$, whereas the same strategy is used to avoid reflections from boundaries in the y direction, and both sides hold 30 grid points as boundary layers (totally there are 360 grid points), with resolution from 250 to $10^4\,m$. In the vertical direction, there are 190 z-levels with $2\,m$ resolution in the upper 175 layers followed by 15 bottom layers with $10\,m$ resolution. Note that as indicated by the modal function, see figure 3, the maximum vertical excursion should occur at approximately depth $h = 165\,m$, which is covered by the fine resolution. Time step is $2\,s$, short enough compared with the typical temporal scale of a mode-1 ISW.

To be succinct, here we only show the results with the truncated initial condition, which can be observed more often in the real ocean. As the KdV-type solitary wave, given by equation (36), is not fully compatible with the Boussinesq equations solved by the MITgcm model (although for small-amplitude waves which are in a weakly nonlinear regime, the difference is very small), thus a 2D simulation is first conducted on a flat bottom (depth $h = 500\,m$) environment with a KdV solitary wave as the initial incident wave, using the background profiles in figure 3. Then we let the wave evolve until it reaches a new stable solution, which is cut off and ready to be used. Essentially in the y direction, it is not easy to impose a smooth envelope on the initial solitary wave in the MITgcm 3D simulations, as described in equation (36). A compromise method is to copy this preliminary 2D solution to fill a central region whose y-direction width is almost the same as the central part of the envelope given in equation (37), whereas the other areas are assumed to be at rest. But these sudden jumps between the initial wave and its periphery will undoubtedly modulate the dynamics to some extent. Indeed, the discrepancy induced by the initial conditions is significant within several hours after the model launches, but nevertheless then a good agreement between the MITgcm and the vKP theory is achieved, see figure 11.

To further examine the robustness of the vKP simulations, the locations of the wavefronts in the x-y space at four different time layers are depicted in figure 11, and these demonstrate that overall a good agreement holds between the vKP simulations and the MITgcm model, except that the curvatures of the wave fronts in the vicinity of canyon (or plateau) topographic features are more abrupt in the KP simulation, which can be partly ascribed to the interpolation used when that is transformed back from the mapping space to the physical space. To make this claim more robust, a quantitative comparison in the amplitude A is also shown in figure 11, in which the wave amplitude of the MITgcm model is calculated using a mode decomposition technique developed by Yuan et al. (2017), which was originally derived in a 2D (x-z) domain. Howeve, since here the y-variations are assumed to be much slower than the x-variations, this technique can be applied in any (x-z) section lines without too much loss of accuracy. Here we will briefly introduce the derivation for our mode-1 wave, there are more details in Yuan et al. (2017). Starting from equation (2), along one (x-z) section line we have

$$c\int_{-h}^{0} \zeta_z \phi_z \, dz = \Lambda S, \quad S = c\int_{-h}^{0} \phi_z^2 \, dz, \tag{41}$$

where Λ is the calculated amplitude in the MITgcm model (as shown in figure 11). Note that in (41) the vertical displacement ζ can not be achieved directly from the model output, and also the z-derivative is not easy in practice, so an alternative (asymptotically) equivalent form will be implemented. In the linear long wave approximation

$$\zeta_t \approx w, \tag{42}$$

which can be combined with the conservation of mass equation

$$u_x + w_z = 0, \tag{43}$$

to yield

$$u_x \approx -\zeta_{tz}\,. \tag{44}$$

Then, also noting that to leading linear long wave order, $\zeta_t + c\zeta_x \approx 0$, the final approximate expression for Λ is

$$\Lambda S \approx \int_{-h}^{0} u\phi_z\, dz\,, \tag{45}$$

where u is the particle velocity in the primary wave propagation (here x) direction, one of the standard outputs from the MITgcm model. We see that the agreement is good, implying that here the variable coefficient KP model and the accompanying analytical interpretations are quite robust.

5. Summary and discussion

The vKP model can be widely applied to the real ocean, under the assumption that the y-variations are much slower than those in the propagation x-direction. In the simulations reported here we have considered 2D bathymetry which is either a submarine canyon or a submarine plateau, these being prototypes of more complicated topographic scenarios. For slowly-varying solitary waves, if there are no y-variations, then from the well-known KdV theory the evolution scenarios of ISWs can be expressed by the adiabatic law $a \propto |\nu|^{1/3}$ relating the amplitude a with the nonlinear coefficient ν, assuming that, as here, ν does not change sign. However, when y-variations are taking into consideration, then an additional spreading effect in the y direction, characterised by a propagation speed proportional to $\nu^{1/3}\theta_0^{1/3}(16\tau/3)^{1/2}$ and a diffusion scale $y_d^2/\varsigma \sim \tau/(\nu^{2/3}\theta_0^{1/3})$, will also play a crucial role. Our simulations show that this can even be overwhelmingly dominant, depending on the initial conditions, such as in our two cases shown in figure 4. But when the initial KdV solitary wave is y-independent in the flat bottom region before the topographic slope, then a very complicated scenario of evolution occurs, which can be explained by the asymptotic theory of the slowly varying solitary wave, combined with the creation of a trailing shelf, induced by mass conservation in the X direction.

For the submarine canyon-type and plateau-type bathymetry, our numerical simulations are performed on the transformed equation (17) which indicates that the essential dynamics are controlled by the transformed coefficients ν and τ, representing the effects of nonlinearity and transverse diffraction respectively. For the simulations reported here, we have found that the former is the more effective. We have developed an asymptotic theory of a slowly varying solitary wave which can be used to examine the effect of y-variations in these coefficients. In particular we have found that the nonlinear phase speed W (25) has a tendency to oppose the change of the corresponding linear phase speed c due to the y-variations in the topography, although the nonlinear correction term $W\lambda$ is too small to fully compensate the change in c, as the ratio is typically $\mathscr{O}(10^{-1})$. That is the phase speed (in the physical space) $c_{sol} \approx c(1+W\lambda)$ is essentially determined by c.

Further, we have found very good agreement between the vKP simulations and simulations using the MITgcm model, both qualitatively and quantitatively. Note that if we were to simplify our continuous stratification to a two-layer structure, using the modal function shown in figure 3, the thickness of the upper layer and lower layer could be estimated as $h_1 = 165\,m$ and h_2 from 185 to $335\,m$ respectively in the whole domain. Since our initial wave amplitude is $15\,m$, then the nonlinearity parameter $a/h_{1,2}$ is $\mathscr{O}(10^{-1})$ and the non-dimensional wavelength $\Delta/h_{1,2}$ (refer to figure 11) is $\mathscr{O}(10^{1})$, which formally satisfies the weakly nonlinear long-wave assumptions. But we note that Ostrovsky and Stepanyants (2005) conducted a series of comparisons between the laboratory experiments and theoretical models and concluded that in some circumstances, the KdV equation, the one-dimensional version of the KP equation, is still adequate for the large amplitude ISWs, beyond the formal range of validity. To some extent the theory can be extended to larger amplitudes by incorporating a cubic nonlinear term, but this may also require additional diffraction terms, and at present such a model is not available. Also, the vKP model is restricted to a single mode, here mode-1, and so cannot describe secondary generation of mode-2 waves, such as those found by Shroyer et al. (2010); Liu et al. (2013). Finally, as found by Ostrovsky (1978); Helfrich (2007); Grimshaw and Helfrich (2008), in some circumstances, the effect of the Earth's background rotation may be quite important. This can be incorporated into the present vKP theory, see for instance Grimshaw (1985); Grimshaw and Melville (1989), but here the rotational effect can be neglected, since according to Farmer et al. (2009); Grimshaw et al. (2012), the importance of the rotation can be measured by the Ostrovsky number, essentially a ratio of the nonlinear term to a rotational term, and when written in the coefficients α, β, $O_s = 2c\alpha^2 a^2/(\beta f^2) \sim \mathscr{O}(10^3) \gg 1$, where f is the Coriolis frequency chosen at latitude 40° N (refer to figure 1). Thus we conclude that here the effect of the background rotation can be neglected.

Acknowledgments. Chunxin Yuan was supported by the Chinese Scholarship Council and UCL Dean's prize. Roger Grimshaw was supported by the Leverhulme Trust through the award of a Leverhulme Emeritus Fellowship. Xueen Chen was supported by the Taishan scholars program as well as Project 2016YFC1401300 of National Key Research and Development Plan and Project 41276008 of Natural Science Foundation of China.

References

Akylas, T., 1994: Three-dimensional long water-wave phenomena. *Annual review of fluid mechanics*, **26 (1)**, 191–210.

Cai, S., and J. Xie, 2010: A propagation model for the internal solitary waves in the northern south china sea. *Journal of Geophysical Research: Oceans*, **115 (C12)**.

Chen, Y., and P. L.-F. Liu, 1995: The unified kadomtsev–petviashvili equation for interfacial waves. *Journal of Fluid Mechanics*, **288**, 383–408.

Da Silva, J. C. B., A. L. New, and J. M. Magalhaes, 2009: Internal solitary waves in the mozambique channel: Observations and interpretation. *Journal of Geophysical Research: Oceans*, **114 (C5)**.

Farmer, D., Q. Li, and J.-H. Park, 2009: Internal wave observations in the south china sea: The role of rotation and non-linearity. *Atmosphere-Ocean*, **47 (4)**, 267–280.

Farmer, D., and J. D. Smith, 1978: Nonlinear internal waves in a fjord. *Elsevier Oceanography Series*, **23**, 465–493.

Grimshaw, R., 1981: Evolution equations for long, nonlinear internal waves in stratified shear flows. *Studies in Applied Mathematics*, **65 (2)**, 159–188.

Grimshaw, R., 1985: Evolution equations for weakly nonlinear, long internal waves in a rotating fluid. *Studies in Applied Mathematics*, **73 (1)**, 1–33.

Grimshaw, R., J. C. da Silva, and J. M. Magalhaes, 2017: Modelling and observations of oceanic nonlinear internal wave packets affected by the earths rotation. *Ocean Modelling*, **116**, 146 – 158.

Grimshaw, R., and K. Helfrich, 2008: Long-time solutions of the ostrovsky equation. *Studies in Applied Mathematics*, **121 (1)**, 71–88.

Grimshaw, R., and W. K. Melville, 1989: On the derivation of the modified kadomtsev-petviashvili equation. *Studies in Applied Mathematics*, **80 (3)**, 183–202.

Grimshaw, R., E. Pelinovsky, and T. Talipova, 1997: The modified korteweg-de vries equation in the theory of large-amplitude internal waves. *Nonlinear Processes in Geophysics*, **4 (4)**, 237–250.

Grimshaw, R., E. Pelinovsky, and T. Talipova, 2007: Modelling internal solitary waves in the coastal ocean. *Surveys in Geophysics*, **28 (4)**, 273–298.

Grimshaw, R., E. Pelinovsky, T. Talipova, and A. Kurkin, 2004: Simulation of the transformation of internal solitary waves on oceanic shelves. *Journal of physical oceanography*, **34 (12)**, 2774–2791.

Grimshaw, R., E. Pelinovsky, T. Talipova, and O. Kurkina, 2010: Internal solitary waves: propagation, deformation and disintegration. *Nonlinear Processes in Geophysics*, **17 (6)**, 633.

Grimshaw, R. H. J., K. Helfrich, and E. R. Johnson, 2012: The reduced ostrovsky equation: integrability and breaking. *Studies in Applied Mathematics*, **129 (4)**, 414–436.

Helfrich, K. R., 2007: Decay and return of internal solitary waves with rotation. *Physics of fluids*, **19 (2)**, 026 601.

Helfrich, K. R., and W. K. Melville, 2006: Long nonlinear internal waves. *Annu. Rev. Fluid Mech.*, **38**, 395–425.

Huang, X., Z. Chen, W. Zhao, Z. Zhang, C. Zhou, Q. Yang, and J. Tian, 2016: An extreme internal solitary wave event observed in the northern south china sea. *Scientific Reports*, **6**, doi: 10.1038/srep30041.

Jackson, C. R., 2004: An atlas of internal solitary-like waves and their properties, 2nd ed. Tech. rep., Global Ocean Assoc., Alexandria, Va. (Available at http://www.internalwaveatlas.com).

Johnson, R. S., 1980: Water waves and korteweg–de vries equations. *Journal of Fluid Mechanics*, **97 (04)**, 701–719.

Kadomtsev, B. B., and V. I. Petviashvili, 1970: On the stability of solitary waves in weakly dispersing media. *Sov. Phys. Dokl*, **15**, 539–541.

Katsis, C., and T. Akylas, 1987: On the excitation of long nonlinear water waves by a moving pressure distribution. part 2. three-dimensional effects. *Journal of Fluid Mechanics*, **177**, 49–65.

Lamb, K. G., and L. Yan, 1996: The evolution of internal wave undular bores: comparisons of a fully nonlinear numerical model with weakly nonlinear theory. *Journal of physical oceanography*, **26 (12)**, 2712–2734.

Liu, A. K., F.-C. Su, M.-K. Hsu, N.-J. Kuo, and C.-R. Ho, 2013: Generation and evolution of mode-two internal waves in the south china sea. *Continental Shelf Research*, **59**, 18–27, doi: 10.1016/j.csr.2013.02.009.

Marshall, J., A. Adcroft, C. Hill, L. Perelman, and C. Heisey, 1997: A finite-volume, incompressible navier stokes model for studies of the ocean on parallel computers. *Journal of Geophysical Research: Oceans*, **102 (C3)**, 5753–5766.

New, A. L., and J. C. B. Da Silva, 2002: Remote-sensing evidence for the local generation of internal soliton packets in the central bay of biscay. *Deep Sea Research Part I: Oceanographic Research Papers*, **49 (5)**, 915–934.

Osborne, A., T. Burch, R. Scarlet, and Coauthors, 1978: The influence of internal waves on deepwater drilling. *Journal of Petroleum Technology*, **30 (10)**, 1–497.

Ostrovsky, L., 1978: Nonlinear internal waves in a rotating ocean. *Oceanology*, **18 (2)**, 119–125.

Ostrovsky, L., and Y. A. Stepanyants, 2005: Internal solitons in laboratory experiments: Comparison with theoretical models. *Chaos: An Interdisciplinary Journal of Nonlinear Science*, **15 (3)**, 037 111.

Pierini, S., 1989: A model for the alboran sea internal solitary waves. *Journal of physical oceanography*, **19 (6)**, 755–772.

Ramp, S. R., and Coauthors, 2004: Internal solitons in the northeastern south china sea. part i: Sources and deep water propagation. *IEEE Journal of Oceanic Engineering*, **29 (4)**, 1157–1181, doi:10.1109/JOE.2004.840839.

Sandstrom, H., and J. Elliott, 1984: Internal tide and solitons on the scotian shelf: A nutrient pump at work. *Journal of Geophysical Research: Oceans*, **89 (C4)**, 6415–6426, doi:10.1029/JC089iC04p06415.

Shroyer, E. L., J. N. Moum, and J. D. Nash, 2010: Mode 2 waves on the continental shelf: Ephemeral components of the nonlinear internal wavefield. *Journal of Geophysical Research: Oceans*, **115 (C7)**, doi:10.1029/2009JC005605.

Vlasenko, V., and N. Stashchuk, 2007: Three-dimensional shoaling of large-amplitude internal waves. *Journal of Geophysical Research: Oceans*, **112 (C11)**.

Vlasenko, V., N. Stashchuk, and K. Hutter, 2005: *Baroclinic tides: theoretical modeling and observational evidence*. Cambridge University Press.

Yuan, C., R. Grimshaw, and E. Johnson, 2017: The propagation of second mode internal solitary waves over variable topography. *J. Fluid Mech.*, **??**, ??

Zhao, Z., V. Klemas, Q. Zheng, and X.-H. Yan, 2004: Remote sensing evidence for baroclinic tide origin of internal solitary waves in the northeastern south china sea. *Geophysical Research Letters*, **31 (6)**.

LIST OF FIGURES

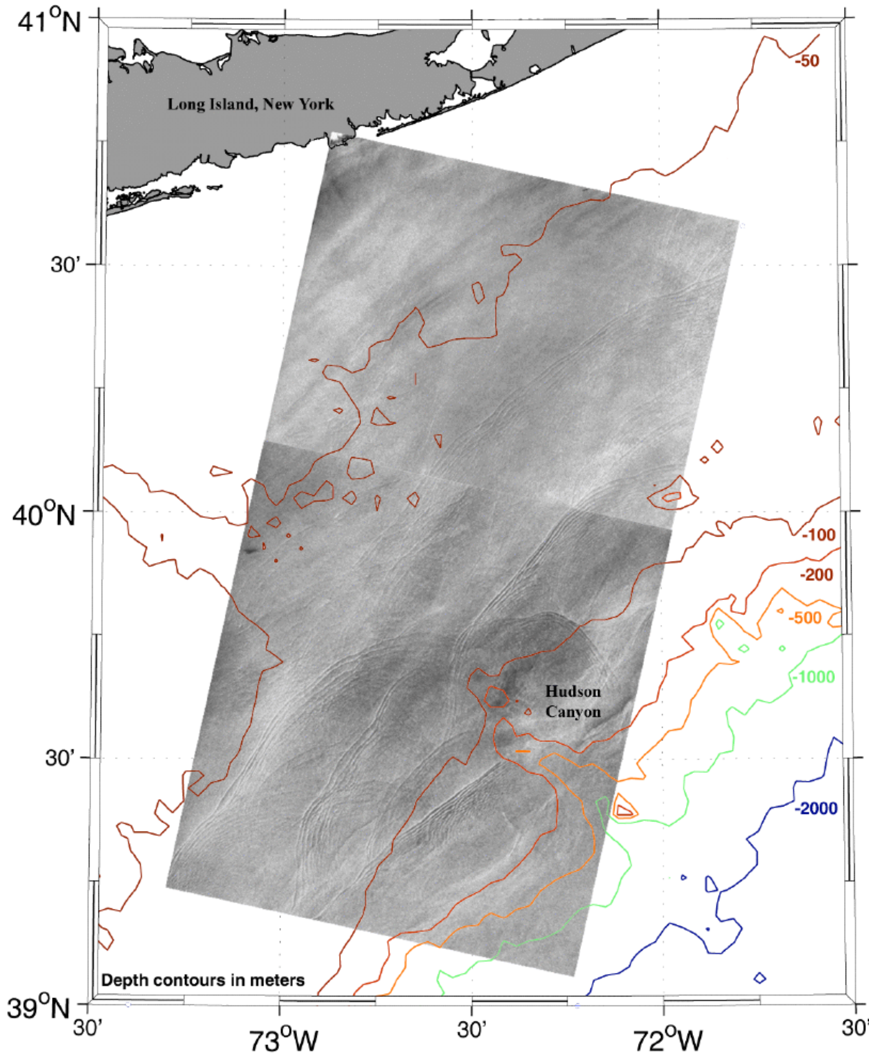

654 FIG. 1. ERS-1 synthetic aperture radar (SAR) images of the New York Bight acquired on 18 July 1992 at 15:35 UTC superimposed on the water depth contour lines. (Figure adapted from Jackson (2004).)

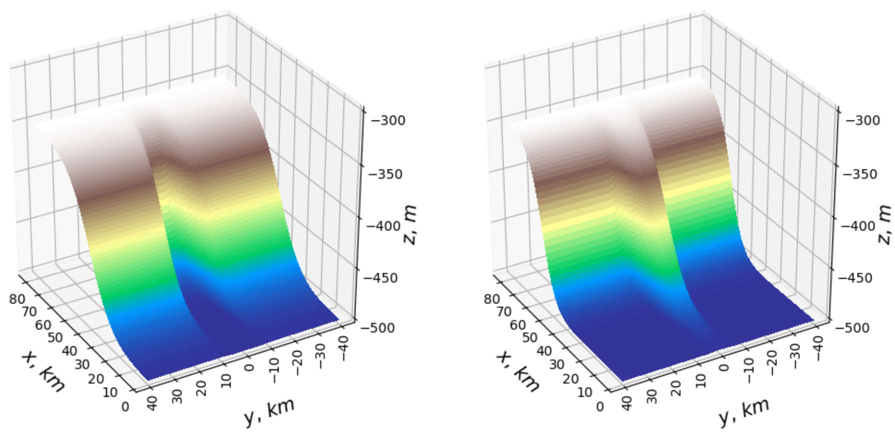

FIG. 2. Canyon-type (left panel) and plateau-type (right panel) topography. For both cases, the depth range is from 350 to 500 m, while the width of the canyon (or plateau) is approximately 20 km.

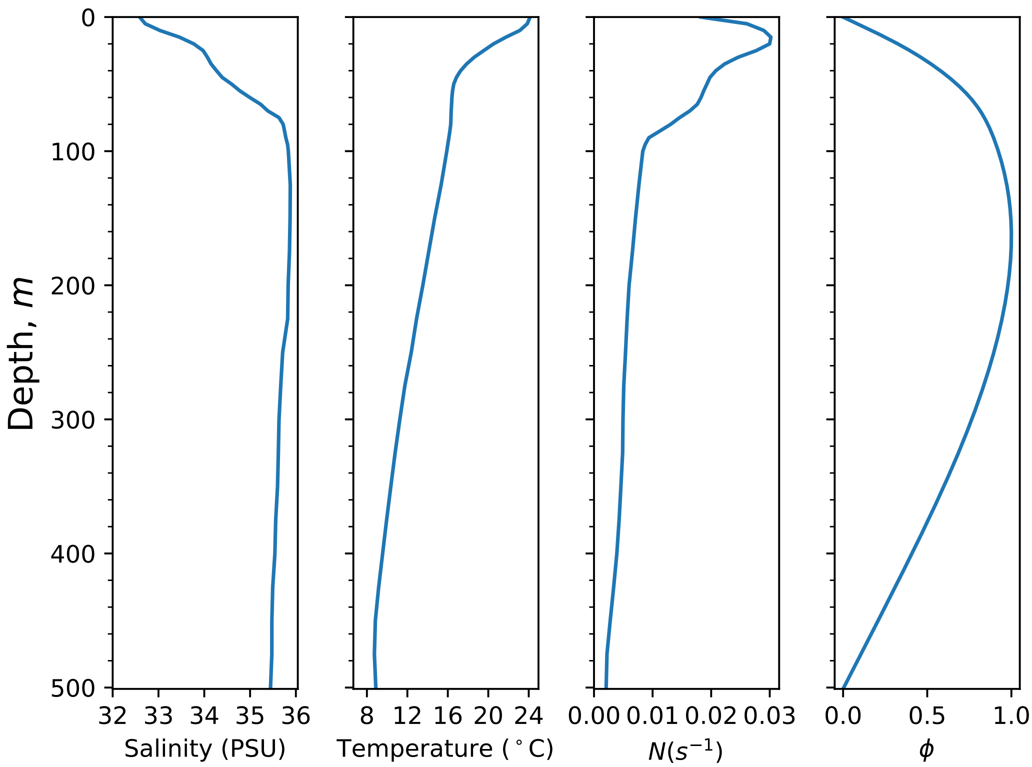

FIG. 3. The panels from left to right are vertical profiles of the salinity, temperature, buoyancy frequency N and corresponding mode-1 modal function ϕ from equation (3, 4) respectively. Note that the extrema of N and ϕ are achieved at depths $h = 16$ and $h = 165\,m$ respectively, which indicates that the most significant internal wave disturbance occurs at a depth where the density gradient is not the largest.

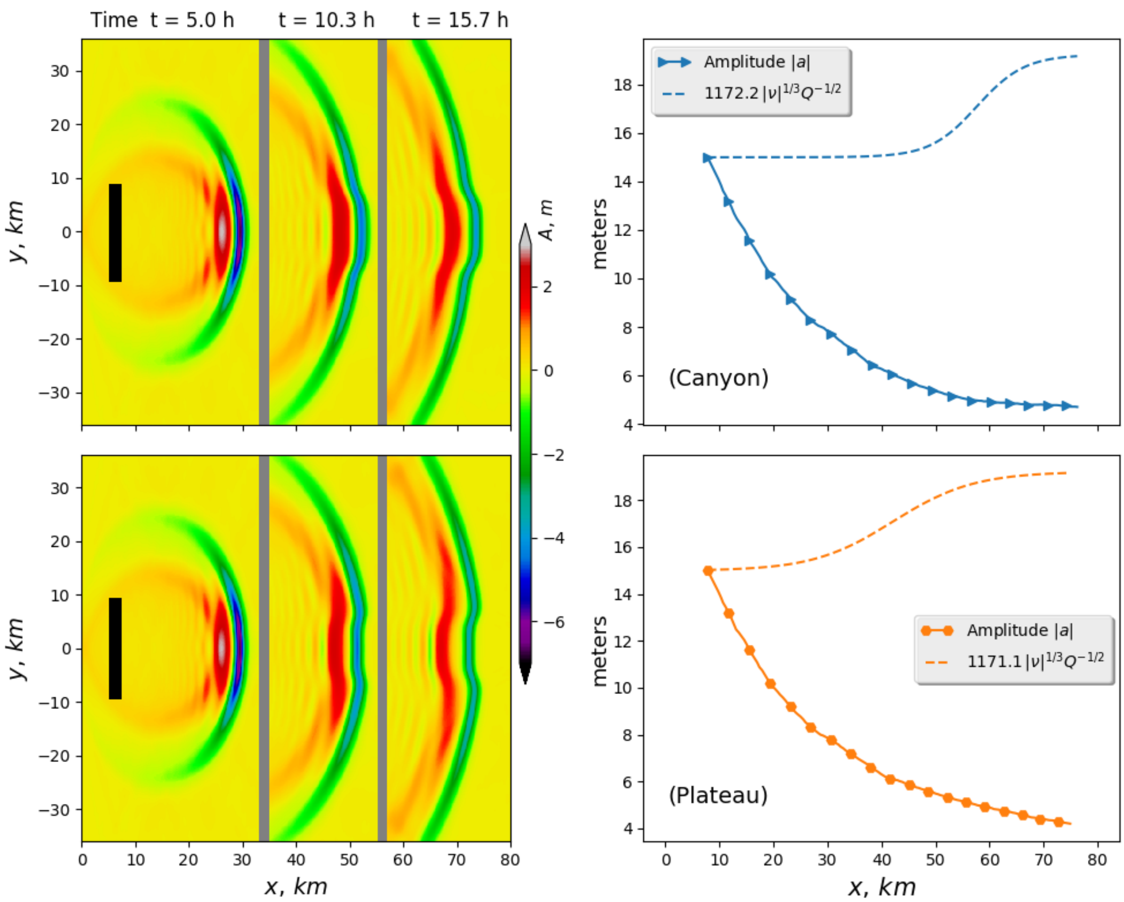

FIG. 4. Three snapshots of the wave amplitude A in equation (11) or (14) for the canyon-type (top left panel) and plateau-type (bottom left panel) topography at times $t = 5.0$, 10.3 and 15.7 hours are illustrated. The initial solitary wave with an amplitude of $-15\,m$ is indicated by a black rectangle, and the results at different times are separated by solid grey columns. The amplitude of the leading wave $|a|$ in the x-direction at the central point $y = 0$, together with the $|\nu|^{1/3}Q^{-1/2}$ times a normalising factor are plotted on the right two panels, where the discrepancy in the evolution of $|a|$ and $|\nu|^{1/3}Q^{-1/2}$ can be attributed to the significant spreading effect in the y direction due to the envelope $E(y)$ imposed on the initial solitary wave.

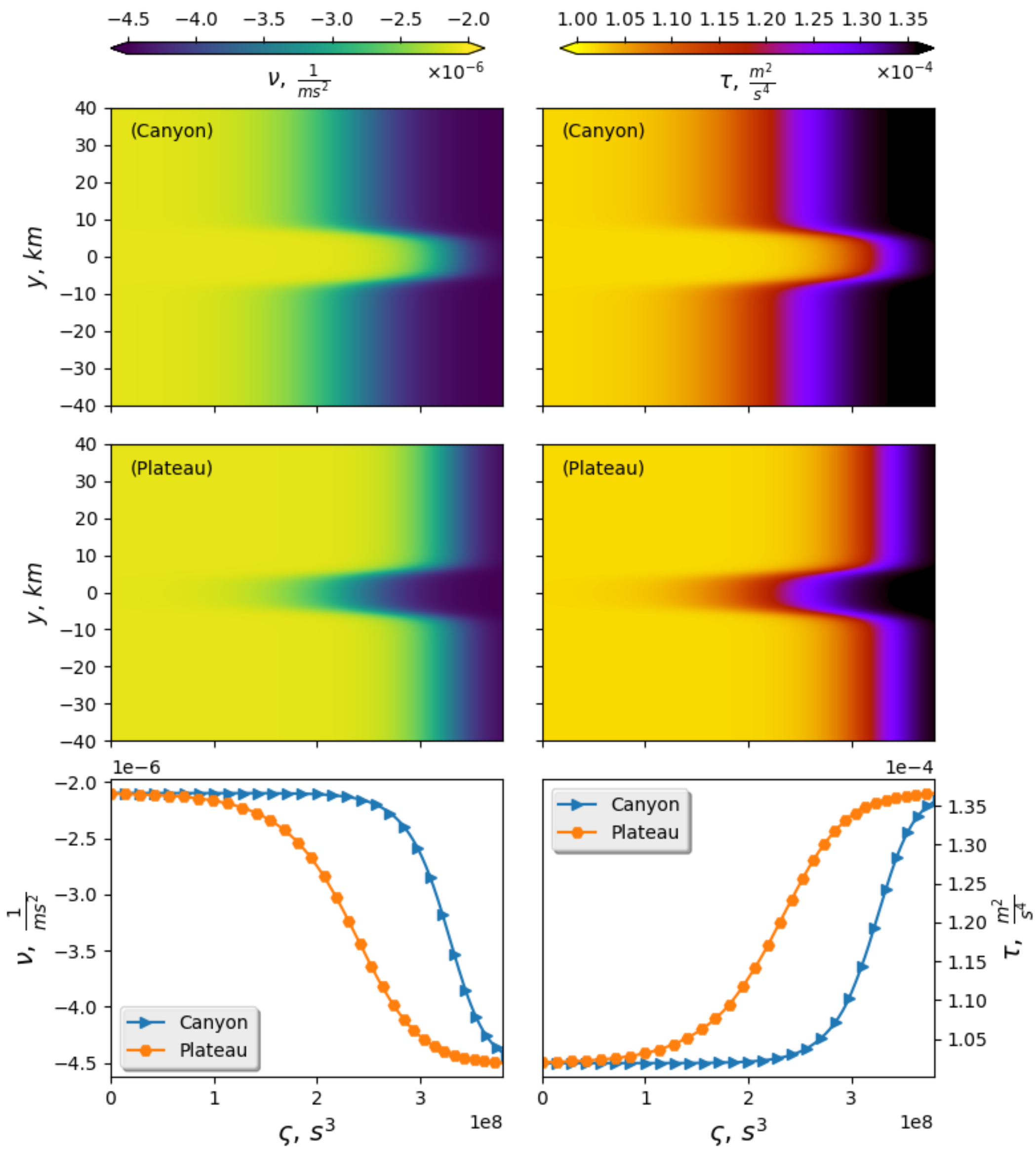

FIG. 5. The nonlinear coefficient ν and the y-dispersive coefficient τ in the transformed space for both the canyon-type and plateau-type topography are shown in the left two and right two panels respectively, whereas the values at the centre point $y = 0$ are displayed on the lowest two panels.

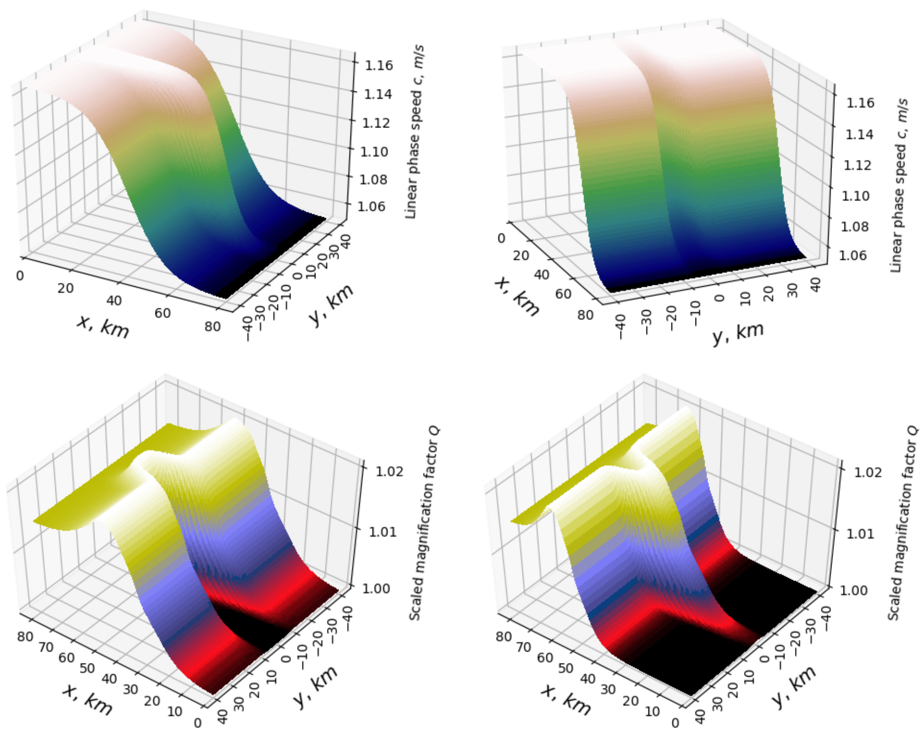

FIG. 6. The linear phase speed c calculated from the modal function (3, 4) for cases of the canyon-type (left top panel) and plateau-type (right top panel) topography. Formally c is positively associated with the water depth h, that is, $c = \sqrt{Nh}$ for internal waves. The bottom two panels are the normalised linear magnification factor Q also for canyon (left) and plateau (right) cases, which are of the same order as c.

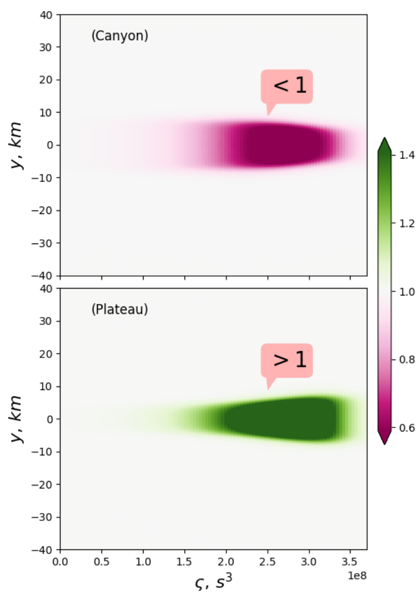

FIG. 7. The dimensionless nonlinear phase speed W with respect to the base level (without y-variations) for the canyon-type and plateau-type topography.

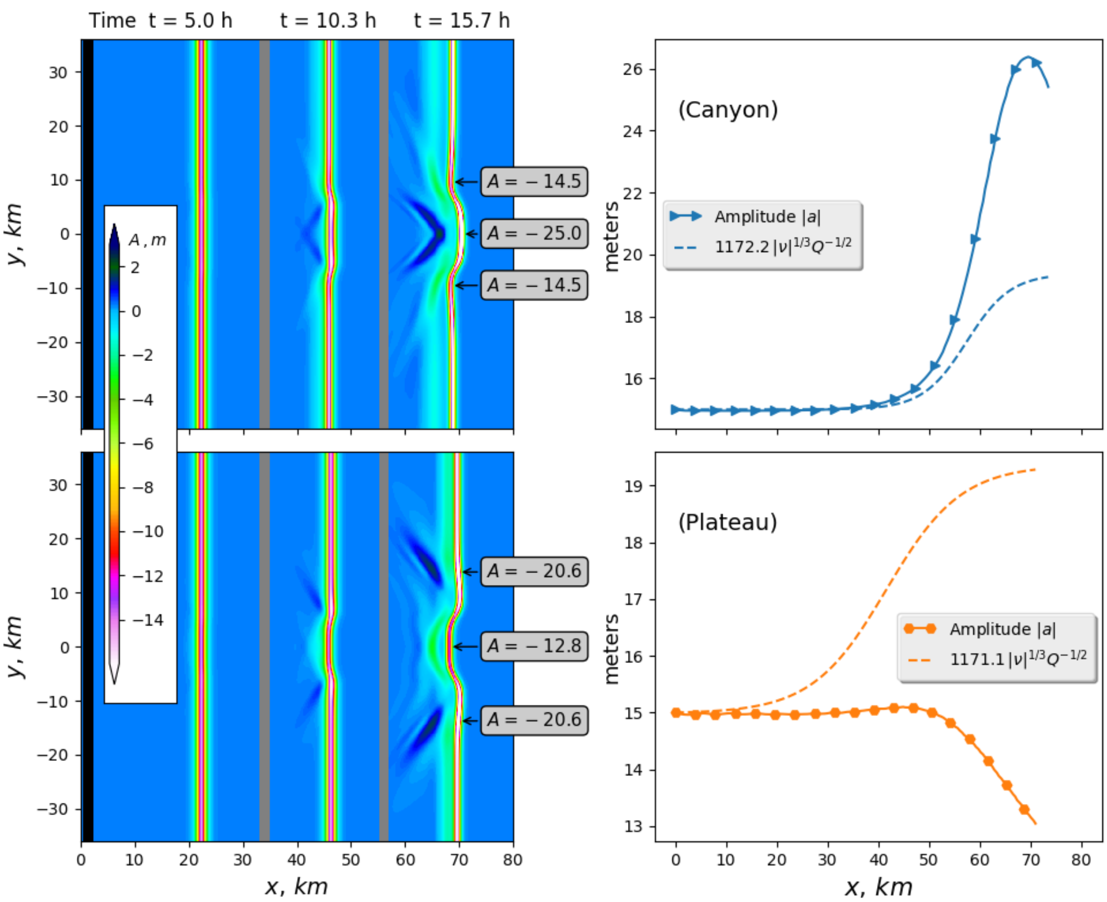

FIG. 8. The left two panels are the wave amplitudes A in equation (11) or (14) for both the canyon-type (top panel) and plateau-type (bottom panel) topography, where three time layers are shown (marked over the pictures), and each of them are separated by grey solid columns. The initial wave with an amplitude of $-15\,m$ is represented by a dark rectangle, which fills all the y domain and enters the region from $x = 0$. In each case, typical wave amplitudes A at three points are listed. The right two panels show the corresponding amplitudes of the leading waves $|a|$ along the central line $y = 0$ in the y direction, and additionally $|\nu|^{1/3}Q^{-1/2}$ times a normalising factor is also plotted.

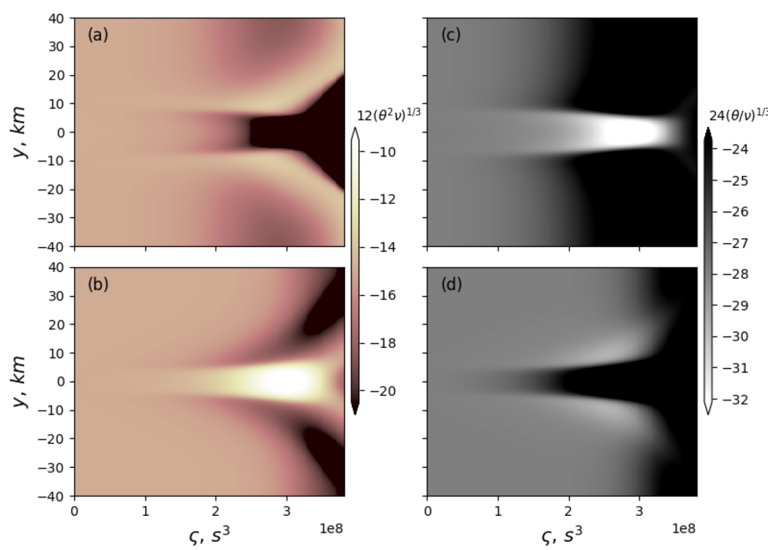

685 FIG. 9. The leading amplitude $a = 12(\theta^2 \nu)^{1/3}$ calculated from equation system (29) in the transformed space for the canyon-type (a) and plateau-type (b) topography, whereas the mass represented by the leading wave $24(\theta/\nu)^{1/3}$ is shown in (c) for the canyon-type topography, (d) for the plateau case.

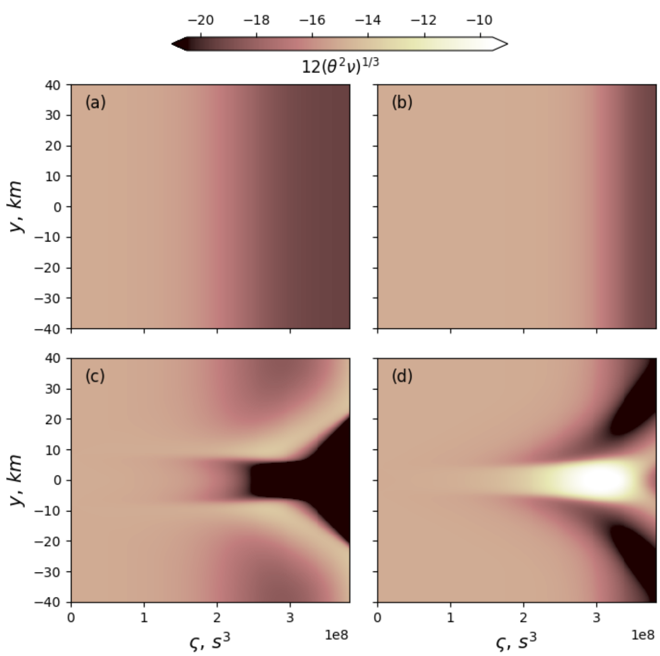

FIG. 10. The leading wave amplitude $a = 12(\theta^2\nu)^{1/3}$ calculated from equation system (29) in the transformed space for the canyon-type ((a) and (c)) and plateau-type ((b) and (d)) topography, where (a) and (b) are the results based on the primitive $\tau(y,\varsigma)$, but a new $\nu(\varsigma)$ whose y-variations are removed. Similarly, (c) and (d) use $\nu(y,\varsigma), \tau(\varsigma)$, in which the y-dependence of τ is erased.

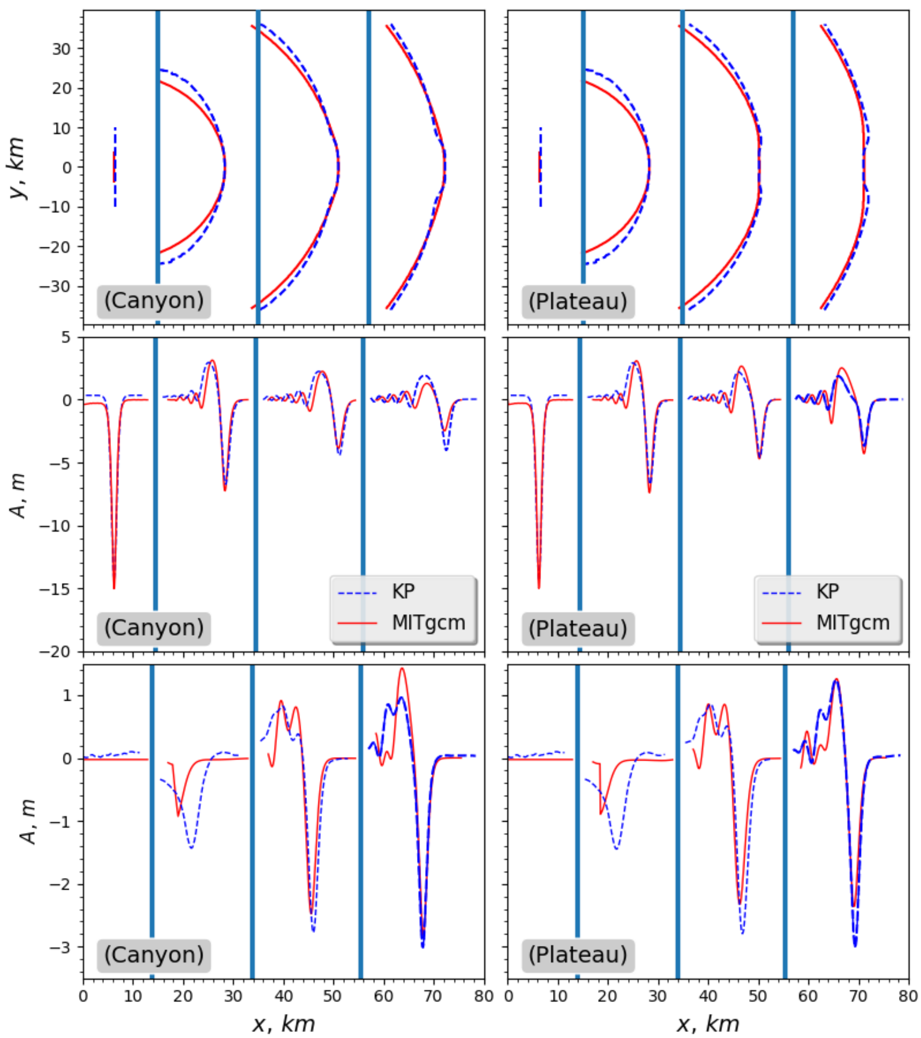

FIG. 11. The top two panels are the locations of the wavefronts from the MITgcm (solid red lines) and the vKP simulations (dashed blue lines) respectively in the cases of canyon-type and plateau-type topography, shown for times at $t = 0.0$, 5.0, 10.3 and 15.7 hours. Selected at the same times, the comparisons of the wave amplitude A on the central line $y = 0$ and the off-centre section $y = 20\,km$ along the x-direction are shown in the middle and bottom two panels respectively.